Effect of spin-dependent tunneling in a $MoSe_2/Cr_2Ge_2Te_6$ van der Waals heterostructure on exciton and trion emission - supplementary materials

Annika Bergmann-Iwe,[1] Swarup Deb,[1,2,3] Klaus Zollner,[4] Veronika Schneidt,[1] Mustafa Hemaid,[1] Kenji Watanabe,[5] Takashi Taniguchi,[6] Rico Schwartz,[1] Jaroslav Fabian,[4] and Tobias Korn[1,*]

[1] *Institute of Physics, Rostock University, 18059 Rostock, Germany*
[2] *Saha Institute of Nuclear Physics, Kolkata, India*
[3] *Homi Bhabha National Institute, Mumbai, India*
[4] *Institute for Theoretical Physics, Regensburg University, 93040 Regensburg, Germany*
[5] *Research Center for Electronic and Optical Materials, NIMS, 1-1 Namiki, Tsukuba 305-0044, Japan*
[6] *Research Center for Materials Nanoarchitectonics, NIMS, 1-1 Namiki, Tsukuba 305-0044, Japan*

S1. SUPPLEMENTARY EXPERIMENTAL DATA

* tobias.korn@uni-rostock.de

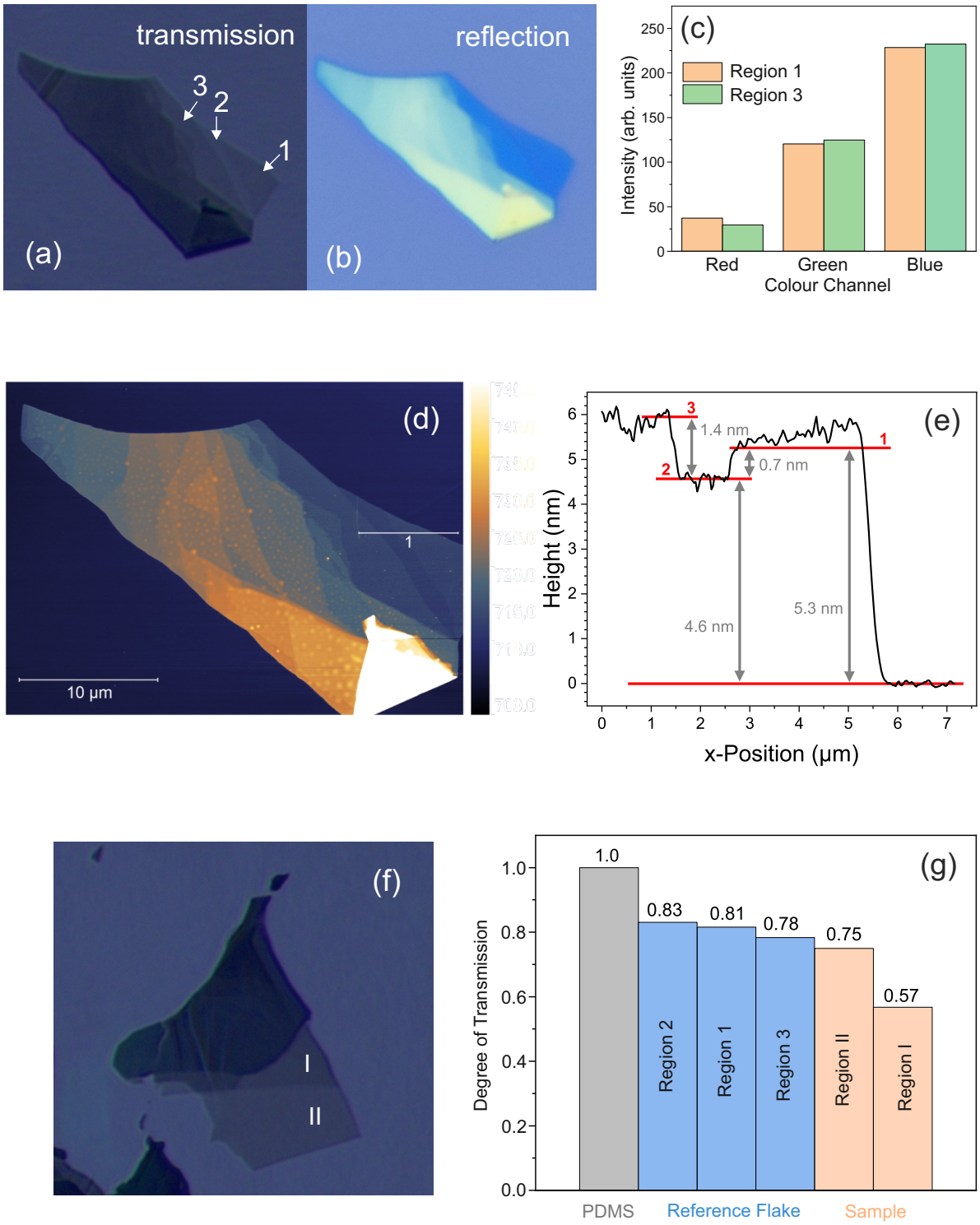

Figure S1 | The CGT sample thickness was determined using a reference sample. (a) The transmission microscopy image of the reference sample on PDMS shows three thin regions (1-3) of different thickness. Here, a clear contrast between 1 and 2 is visible, whereas the contrast between 1 and 3 is poor. The reflection light image (b) of the same sample on a Si/SiO_2 substrate reveals a difference in layer thickness between 1 and 3 which manifests itself in different nuances of blue. The contrast is reflected in all colour channels (c). (d,e) AFM measurements were performed to elucidate the actual sample thickness. Assuming a monolayer step height of 1.1 nm and a step height of 0.7 nm for every subsequent layer in accordance with [1], region 2 consists of 6, region 1 of 7 and region 3 of 8 layers. (f,g) From the transmission microscopy images the degree of transmission for the reference flake and the CGT flake shown in the main text was determined, using the PDMS film as a calibration. We assume a reduction of about 3 percent per layer. A comparison between the values for the flake shown in the main text and the reference flake hints at layer thicknesses of 9 layers in region I and 14 layers in region II.

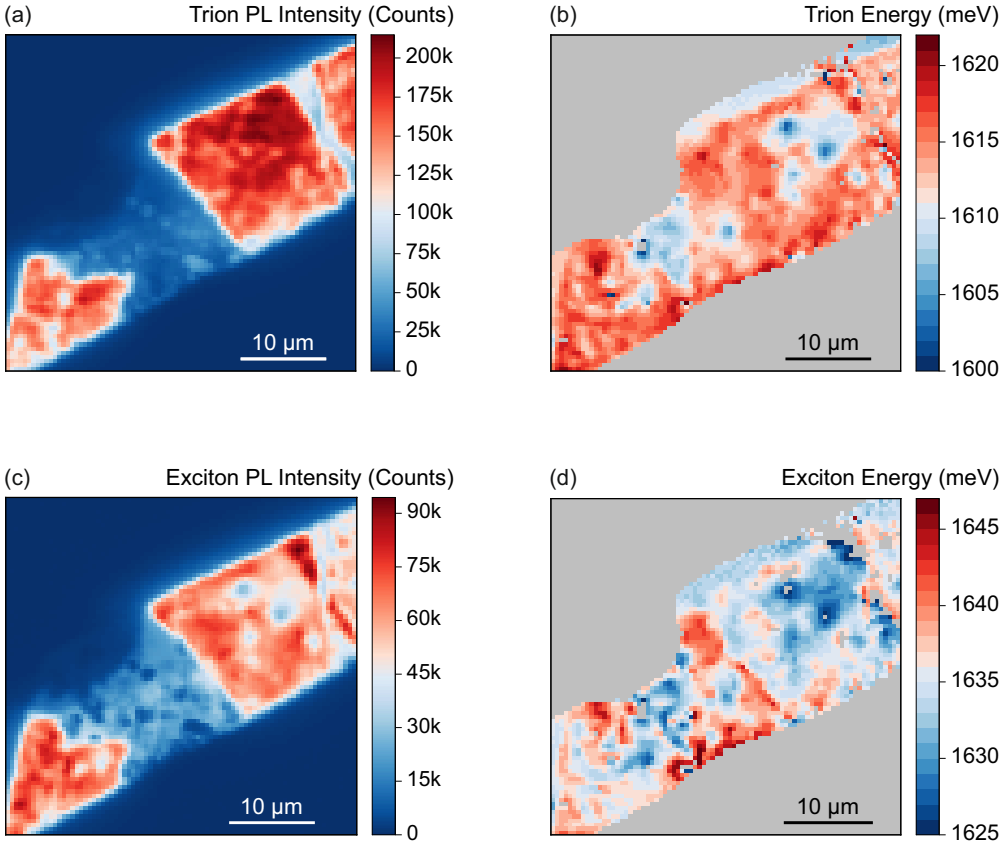

Figure S2 | Photoluminescence scans of the area marked in Fig. S3a. Trion and exciton intensities (a), (c) were obtained by numerical integration over the respective energetic range. Lorentz fits were used to determine the trion and exciton peak positions (b), (d).

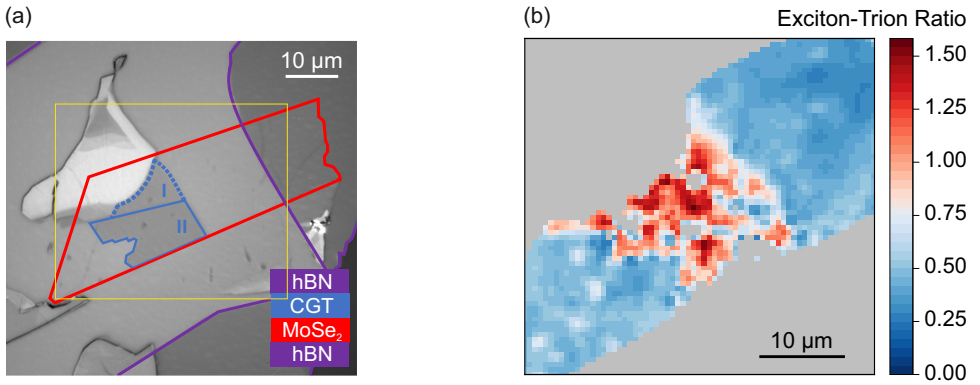

Figure S3 | (a) In the optical microscope image, the yellow box indicates the area shown in the maps obtained from PL scans. The $MoSe_2$ monolayer emission is quenched in the heterostructure region (see main text and Fig. S2). Here, larger exciton-trion ratios are observed compared to the $MoSe_2$ monolayer (b). The strong scatter between occurring ratios is attributed to inhomogeneous interfacial contact between the $MoSe_2$ monolayer and the CGT flake. On average, a slightly larger exciton-trion ratio is observed for region I compared to region II. Due to the large ratio change from monolayer to heterostructure region this is not apparent in the colour map.

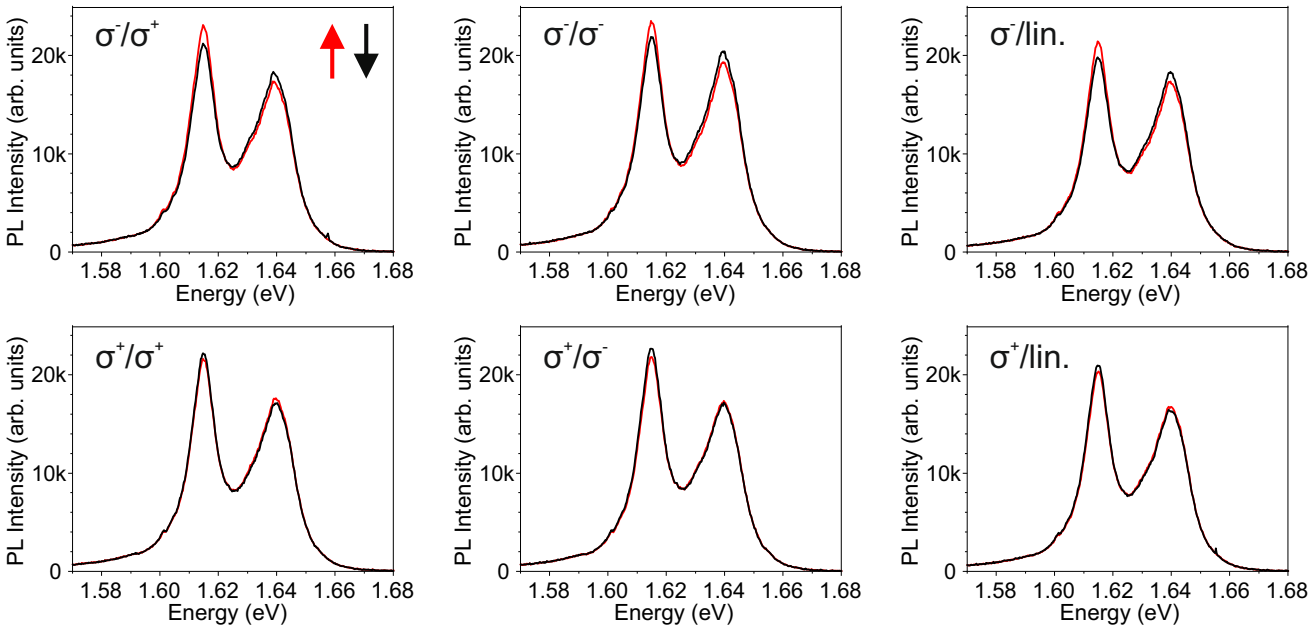

Figure S4 | PL spectra for different (excitation/detection) helicities and magnetic field directions (arrows). For a constant excitation helicity, the population dynamics is independent of the detection helicity. Measurements were conducted at a magnetic field of $\pm 50\,\mathrm{mT}$.

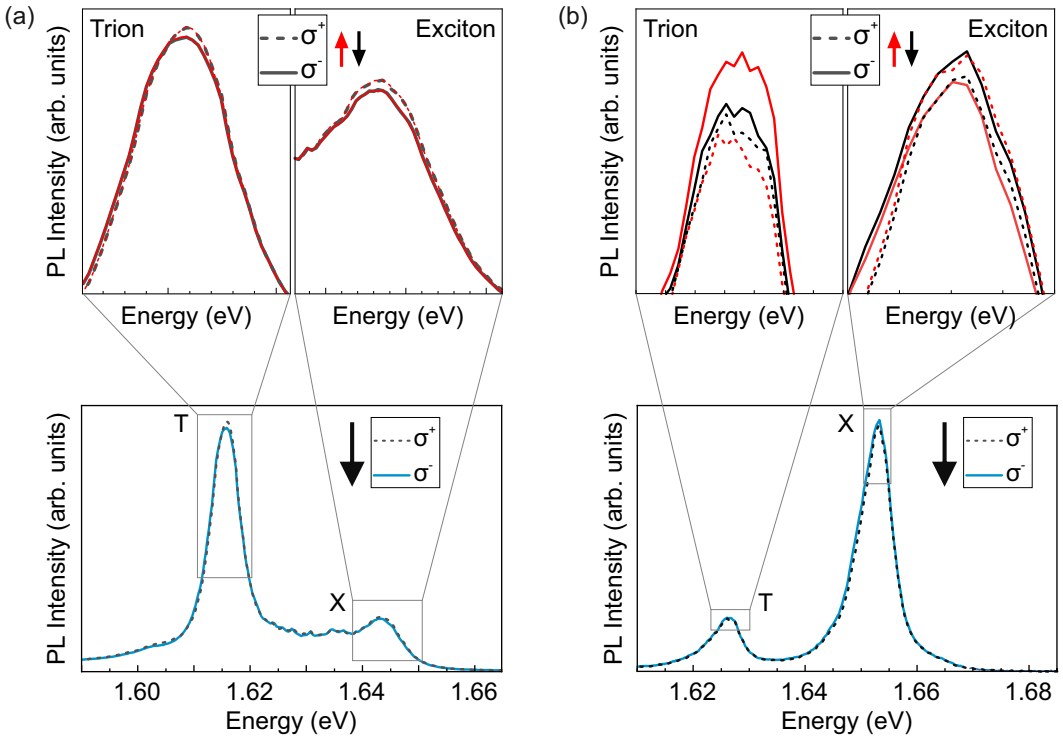

Figure S5 | No magnetic-field-dependent intensity differences for left (solid) and right (dashed line) circularly polarized excitation are detected in the isolated monolayer (a) at a magnetic field of $\pm 50\,\mathrm{mT}$. This proves that the magnetic-field-dependent intensity differences result from an interaction between the $MoSe_2$ monolayer and the overlying CGT layer. For better visibility only the spectra for B↓ are shown in the lower panel. The upper panels show a zoom in of trion and exciton peak for both magnetic field directions. Small intensity differences for left and right polarized excitation result from minor changes of laser excitation spot. In comparison, magnetic-field-dependent changes of exciton and trion intensities occur in the heterostructure (b). The PL spectra were recorded on a second sample that is not shown in the main text.

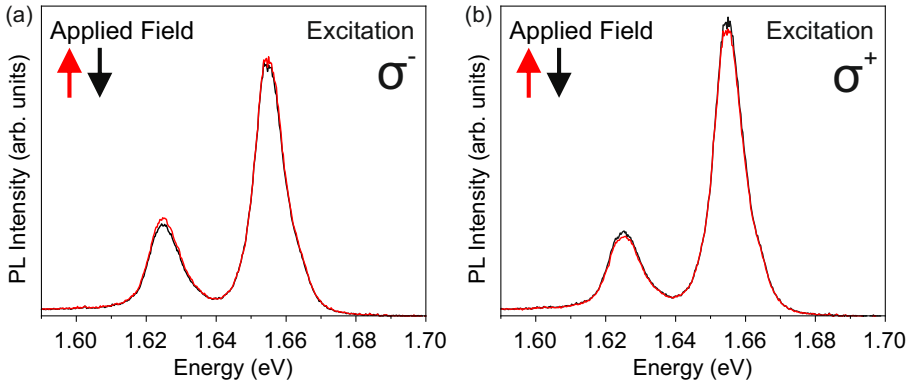

Figure S6 | In a second sample, the effect resulting from spin-dependent tunneling takes on different characteristics. While at some sample positions the relative intensity difference upon flip of the magnetic field is opposite between exciton and trion as discussed in the main text (see Fig. S5b), at other sample positions both exciton and trion emission are suppressed under conditions of enhanced electron tunneling into the CGT layer.

S2. DFT CALCULATIONS ON $MOSE_2/CR_2GE_2TE_6$

A. Structural Setup

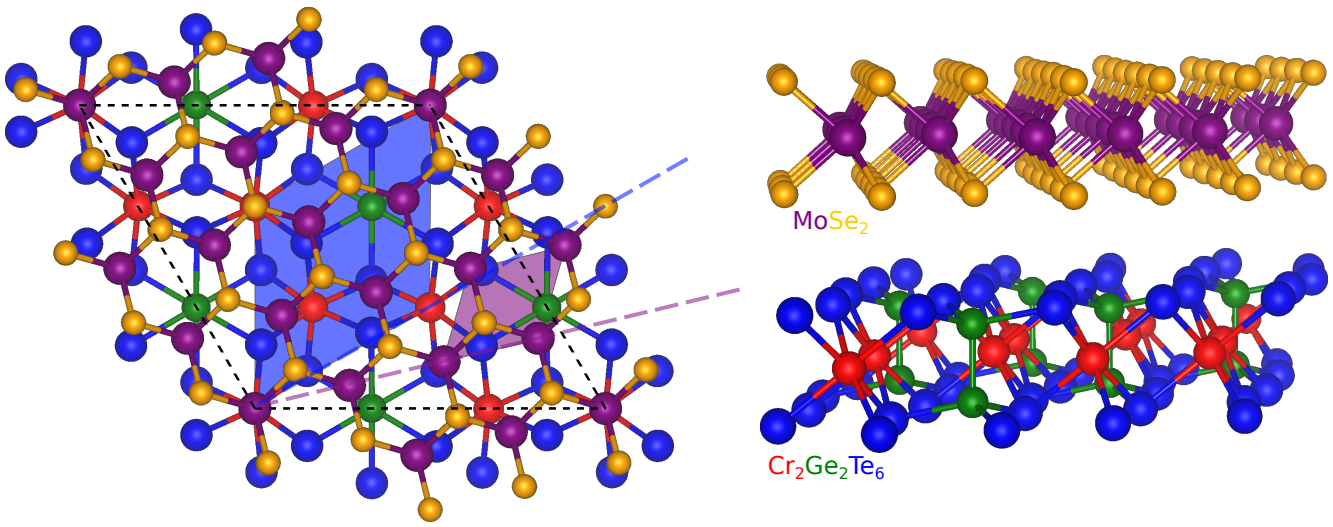

Figure S7 | Top and side view of the $MoSe_2/Cr_2Ge_2Te_6$ heterostructure. The supercell has 69 atoms, with the lattice parameters of $|a| = |b| = 11.855$ Å and $|c| = 34.065$ Å. The relaxed average interlayer distance between the layers is $d = 3.515$ Å. The purple (blue) shaded area indicates the monolayer $MoSe_2$ ($Cr_2Ge_2Te_6$) unit cell, while the black dashed line is the heterostructure unit cell. The twist angle between the layers is 16.102°.

The $MoSe_2/Cr_2Ge_2Te_6$ heterostructure was set-up with the `atomic simulation environment (ASE)` [2] and the `CellMatch` code [3], implementing the coincidence lattice method [4, 5]. The lattice constant of $Cr_2Ge_2Te_6$ within the heterostructure is 6.8445 Å, slightly strained by 0.25% [6]. The $MoSe_2$ layer is kept unstrained with a lattice constant of 3.288 Å [7]. Therefore, the individual monolayers are barely strained in our heterostructure and we should be able to reliably extract band offsets as well as proximity exchange effets. In order to simulate quasi-2D systems, we add a vacuum of about 18 Å to avoid interactions between periodic images in our slab geometry. The resulting heterostructure is shown in Fig. S7.

B. Computational Details

The electronic structure calculations and structural relaxations of the $MoSe_2/Cr_2Ge_2Te_6$ heterostructure is performed by DFT [8] with `Quantum ESPRESSO` [9]. Self-consistent calculations are carried out with a k-point sampling of $24\times24\times1$. We perform open shell calculations that provide the spin-polarized ground state of the $Cr_2Ge_2Te_6$ monolayer. A Hubbard parameter of $U = 1.0$ eV is used for Cr d-orbitals, being in the range of proposed U values especially for this compound [1]. We use an energy cutoff for charge density of 600 Ry and the kinetic energy cutoff for wavefunctions is 75 Ry for the (scalar) relativistic pseudopotentials with the projector augmented wave method [10] with the Perdew-Burke-Ernzerhof exchange correlation functional [11]. For the relaxation of the heterostructures, we add DFT-D2 vdW corrections [12–14] and use quasi-Newton algorithm based on trust radius procedure. To get proper interlayer distances and to capture possible moiré reconstructions, we allow all atoms to move freely within the heterostructure geometry during relaxation. Relaxation is performed until every component of each force is reduced below 5×10^{-4} [Ry/a_0], where a_0 is the Bohr radius.

C. Results

1. *Without Spin-Orbit Coupling*

First, we discuss the first-principles results, where spin-orbit coupling is excluded from the calculations and the magnetization direction of $Cr_2Ge_2Te_6$ is fixed to be collinear with the z-axis (transverse to the interface). In Fig. S8

we show the calculated band structure and density of states (DOS) of the $MoSe_2/Cr_2Ge_2Te_6$ heterostructure. We find that the heterostructure forms a type I band alignment, as the $Cr_2Ge_2Te_6$ band edges reside within the $MoSe_2$ band edges. The calculated dipole of the heterostructure is -0.0542 debye, so there is almost no electric field across the interface. The averaged induced magnetic moments on the different atomic layers are: Cr = 3.484 μ_B, Ge = 0.058 μ_B, Te = -0.192 μ_B, Se_1 = -0.0015 μ_B, Mo = -0.002 μ_B, and Se_2 = -0.0001 μ_B.

In particular the DOS gives a first indication of a strong hybridization of conduction band states. To further confirm this, we have calculated a layer-projected band structure, shown in Fig. S10. The valence band edges of $MoSe_2$ are almost unperturbed within the heterostructure, but the conduction band edge states are rather strongly hybridized. A detailed zoom to the $MoSe_2$ band edges is given in Fig. S11. Due to proximity-induced exchange coupling, the band edges experience spin splittings, as indicated. Since the valence band edge of $MoSe_2$ rather weakly hybridizes (anticrosses) with $Cr_2Ge_2Te_6$ bands, the splitting is about 1.2 meV. In contrast, the conduction band edge of $MoSe_2$ is much stronger hybridized leading to a spin-splitting of about 2.5 meV near the band edge.

Experimentally, the hybridization opens an efficient charge transfer channel for photo-excited charge carriers from $MoSe_2$ into $Cr_2Ge_2Te_6$. Since most of the heterostructure bands below the $MoSe_2$ conduction band edge are spin-up polarized $Cr_2Ge_2Te_6$ bands, a predominant transfer of spin-up polarized electrons is expected. The predominant tunneling of spin-up electrons is supported by the layer-resolved density of states, see Fig. S9.

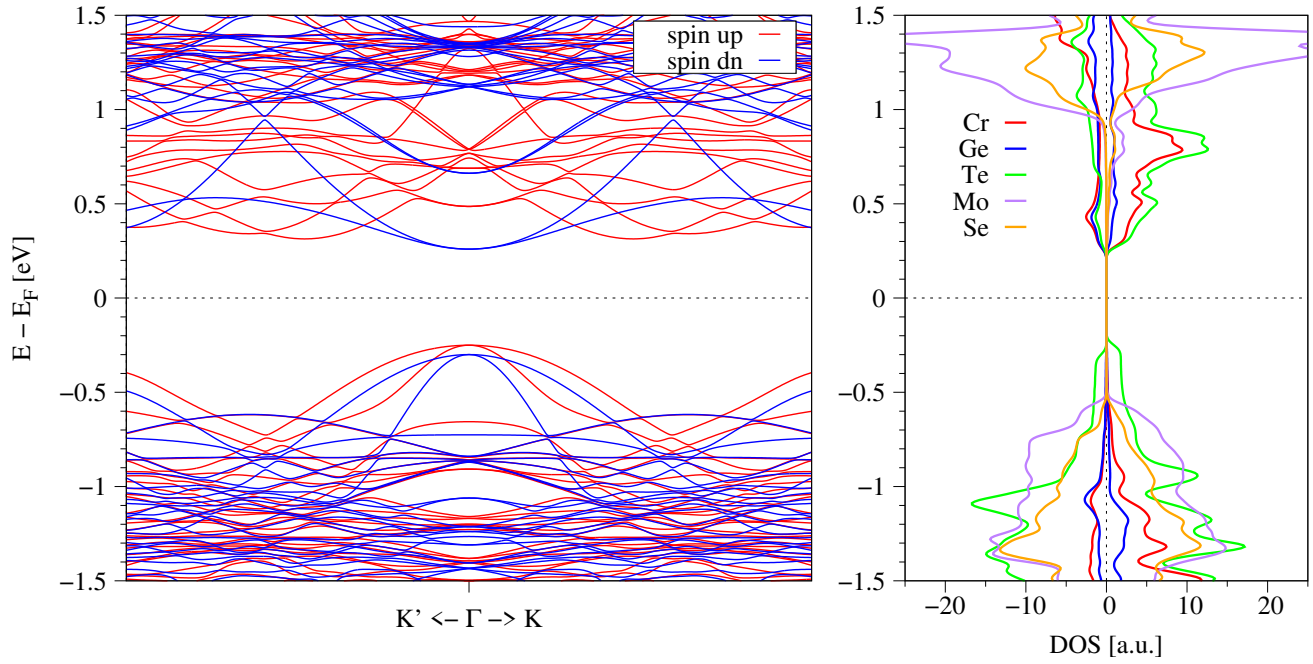

Figure S8 | Left: DFT-calculated band structure of the $MoSe_2/Cr_2Ge_2Te_6$ heterostructure towards the $MoSe_2$ valley edges at K/K'. Red (blue) lines correspond to spin up (down). Right: The corresponding spin and atom resolved density of states. Positive (negative) DOS is for spin up (down).

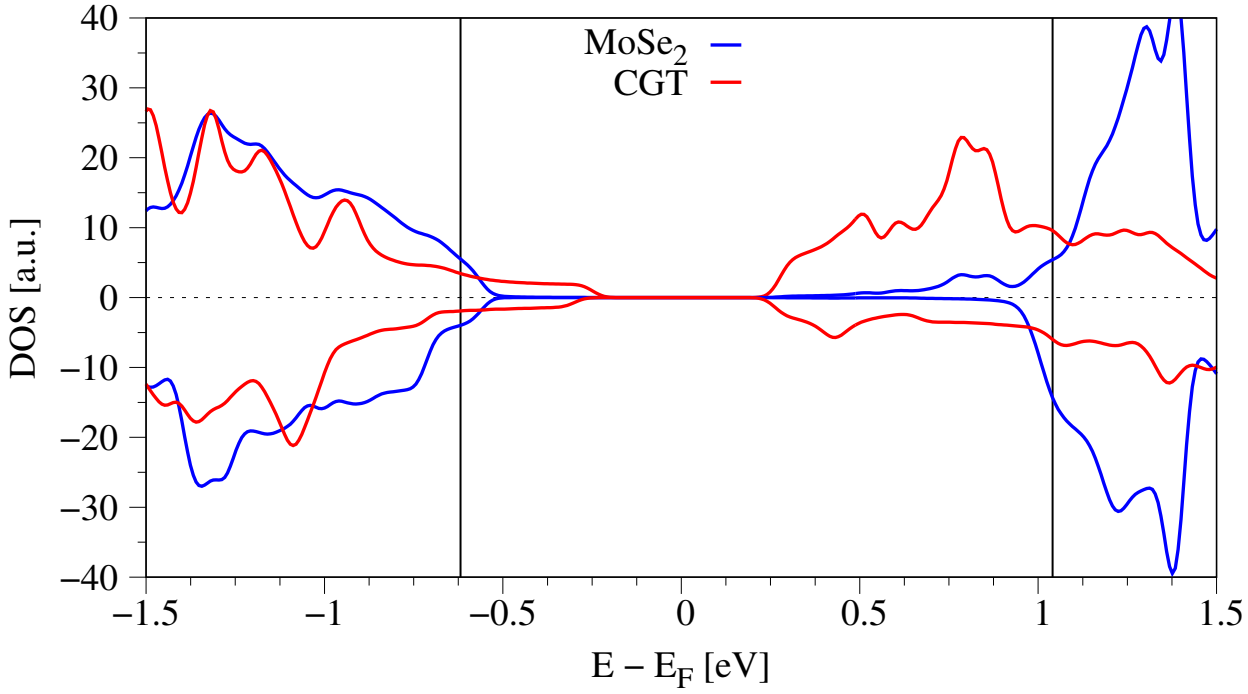

Figure S9 | The calculated layer-resolved density of states of the $MoSe_2/Cr_2Ge_2Te_6$ heterostructure. Positive (negative) DOS is for spin up (down). Black vertical lines indicate the $MoSe_2$ band edges at K/K'.

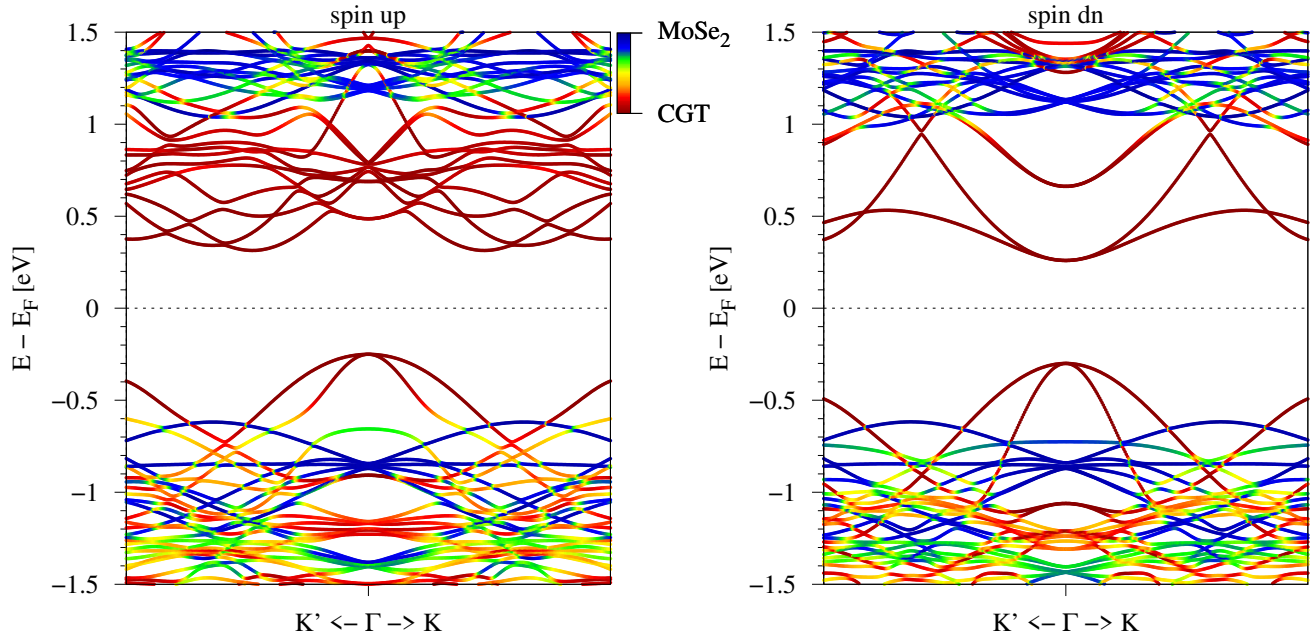

Figure S10 | The layer-projected band structure for spin up (left) and spin down (right) channels. The color code indicates the projection onto the monolayers.

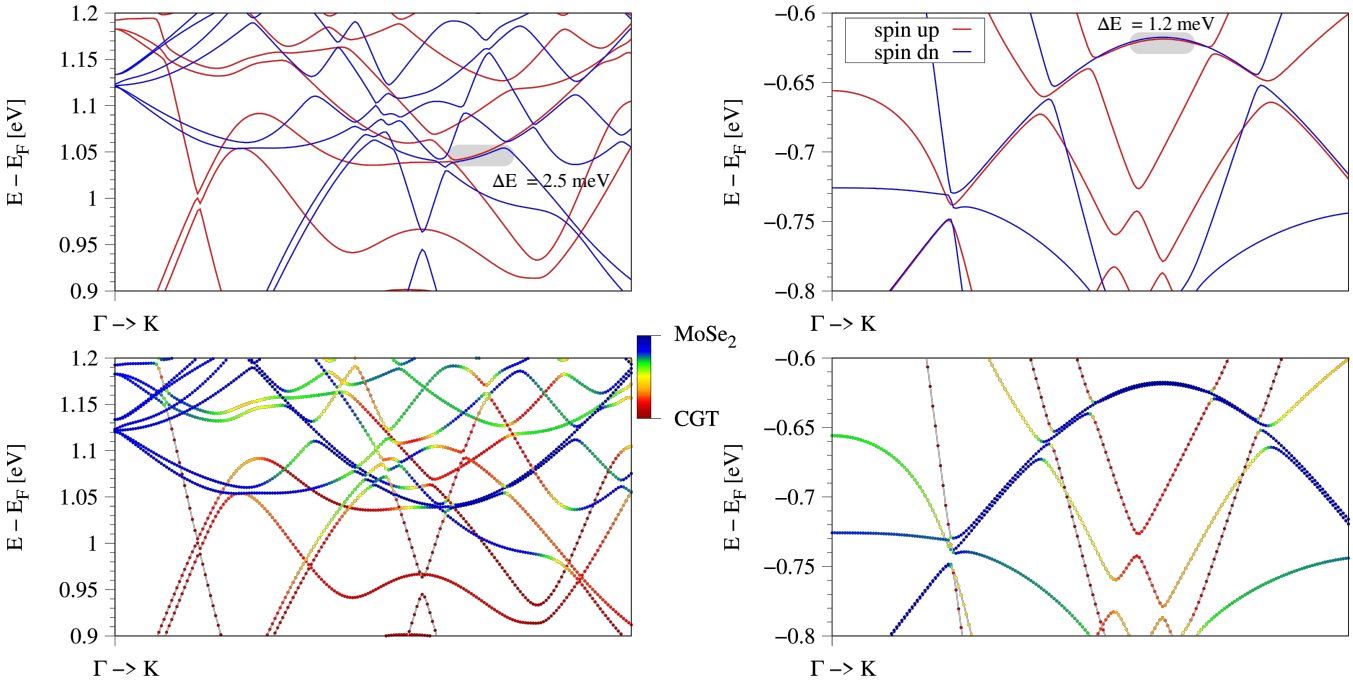

Figure S11 | Zoom to the band edges near the K-valley of $MoSe_2$.

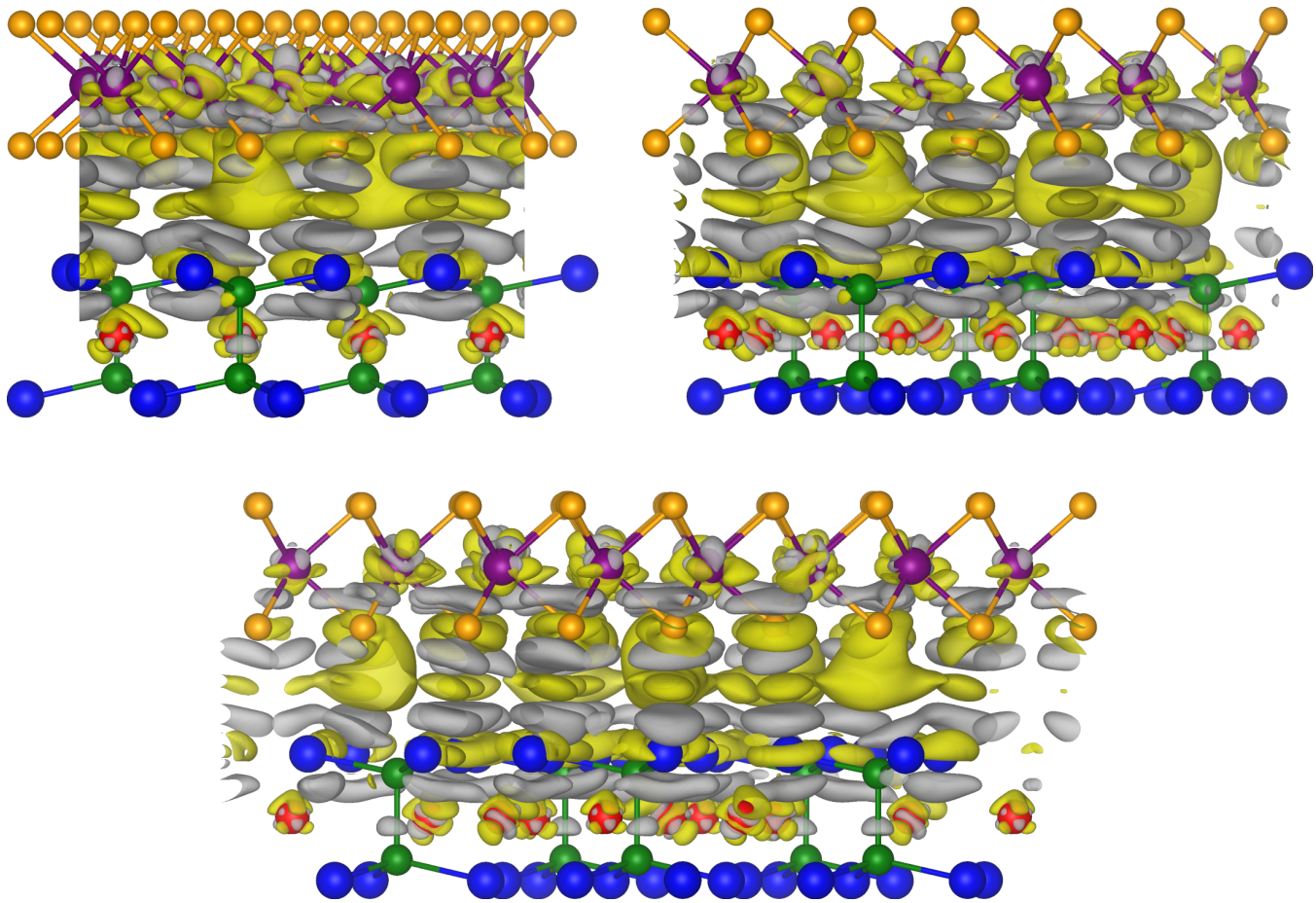

Figure S12 | DFT-calculated charge redistribution, by subtracting the monolayer charge densities from the heterostructure one. The colors yellow and gray correspond to gain and loss of charge. The isovalue is set to 1×10^{-4} e/Å^3.

2. *With Spin-Orbit Coupling, Noncollinear Case*

To get a more realistic description of the heterostructure dispersion, we consider noncollinear magnetism and spin-orbit coupling in the calculations. The reason is that spin-orbit coupling is utterly important for the description of $MoSe_2$. Additionally, the noncollinear calculation allows the atoms to freely adjust their magnetization directions, as interfacial hybridization may disturb the out-of-plane magnetism of $Cr_2Ge_2Te_6$.

In Fig. S13, we show the band structure of the heterostructure including spin-orbit coupling. The type-I band alignment remains, as we find from the layer-projected dispersion. The spin character of the bands is mainly of s_z, indicating that the $MoSe_2$ Ising spin-orbit coupling and the out-of-plane magnetism of $Cr_2Ge_2Te_6$ also remain intact. Zooming into the band edges of $MoSe_2$, see Fig. S14, we find that the valence band edges at K/K' are well preserved, but are energetically split by about 1.6 meV, stemming from the proximity-induced magnetism. In contrast, the conduction band edges can also still be recognized, but are well hybridized. Apart from the additional spin-orbit coupling induced band splittings, the overall picture remains the same, supporting spin-dependent tunneling of photo-excited electrons from $MoSe_2$ into $Cr_2Ge_2Te_6$.

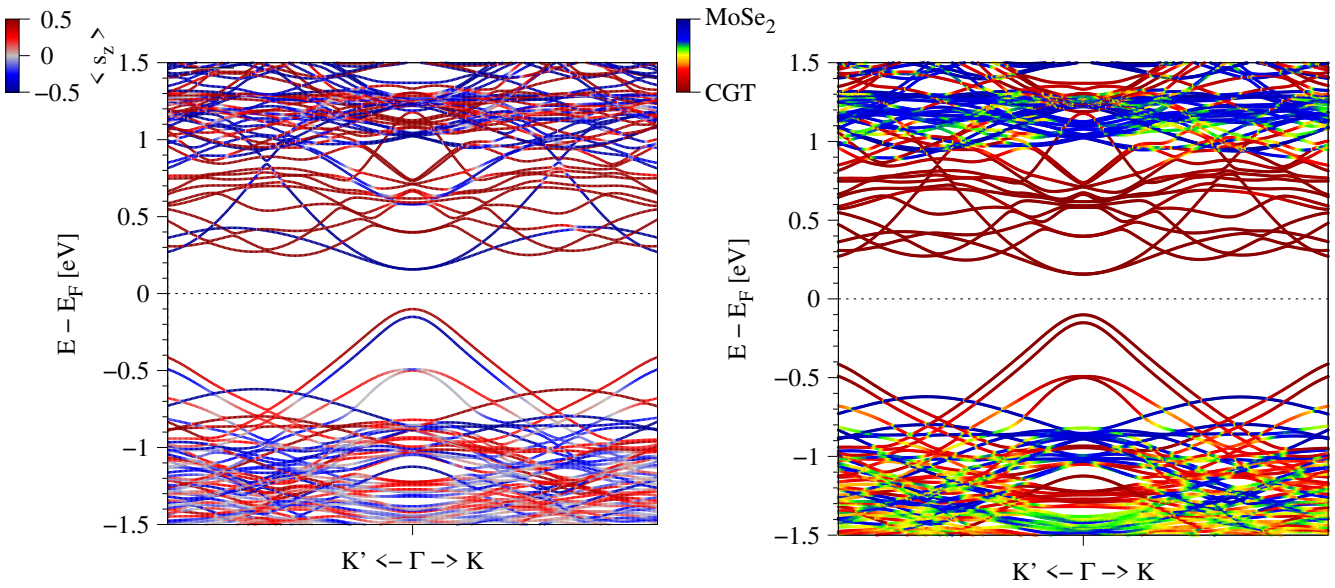

Figure S13 | DFT-calculated band structure of the $MoSe_2/Cr_2Ge_2Te_6$ heterostructure, with spin-orbit coupling and including noncollinear magnetism. We show the bands with s_z and layer projections.

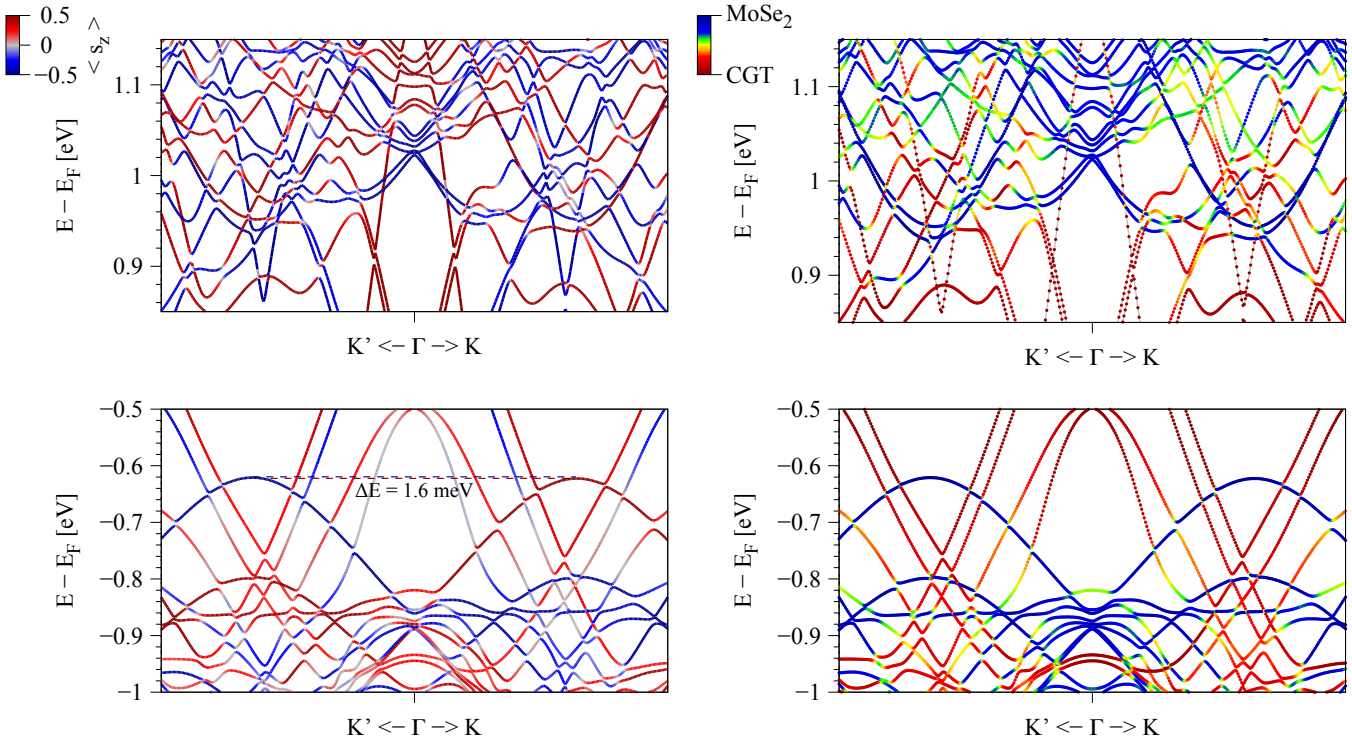

Figure S14 | Zoom to the band edges near K/K' valleys of $MoSe_2$.

3. *Increasing the thickness of the magnet*

Experimentally, $MoSe_2$ is considered on few (9-15) layers of $Cr_2Ge_2Te_6$. Initial experiments on the thickness-dependence of the Curie temperature of $Cr_2Ge_2Te_6$, indicate that this thickness can be regarded as bulk crystal [1]. Computationally it is very demanding to simulate heterostructures, since many atoms are involved in the geometry. However, we know from previous studies that the proximity-coupling is short-ranged and typically restricted to neighboring layers [15]. Therefore, we add a second $Cr_2Ge_2Te_6$ layer beneath the first one, in AB-stacking configuration and without changing the interfacial alignment of the $MoSe_2/Cr_2Ge_2Te_6$ heterostructure, and look for qualitative changes in the results. Before calculating the dispersion, we allow for full structural relaxation of this trilayer system. Based on the results in Figs. S15, S16, S17, and S18, we find barely any qualitative difference to the monolayer case, indicating the short-rangeness of proximity coupling.

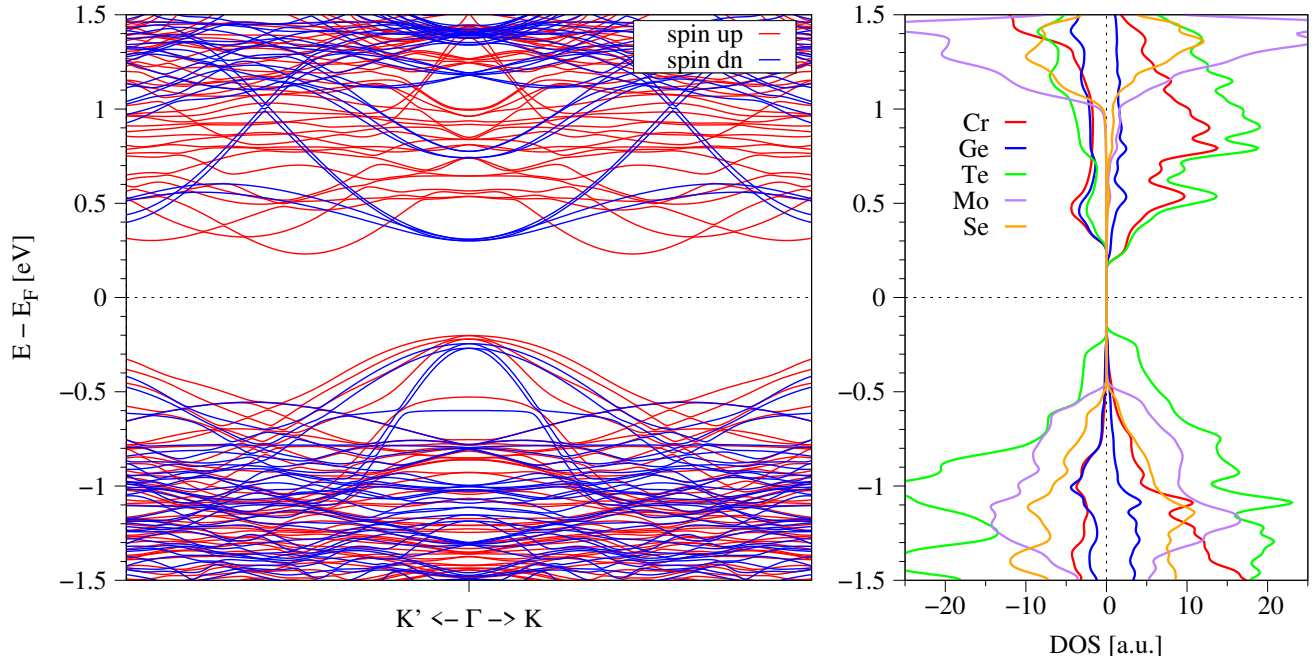

Figure S15 | Left: DFT-calculated band structure of the $MoSe_2$/bilayer-$Cr_2Ge_2Te_6$ heterostructure towards the $MoSe_2$ valley edges at K/K'. Red (blue) lines correspond to spin up (down). Right: The corresponding spin and atom resolved density of states. Positive (negative) DOS is for spin up (down).

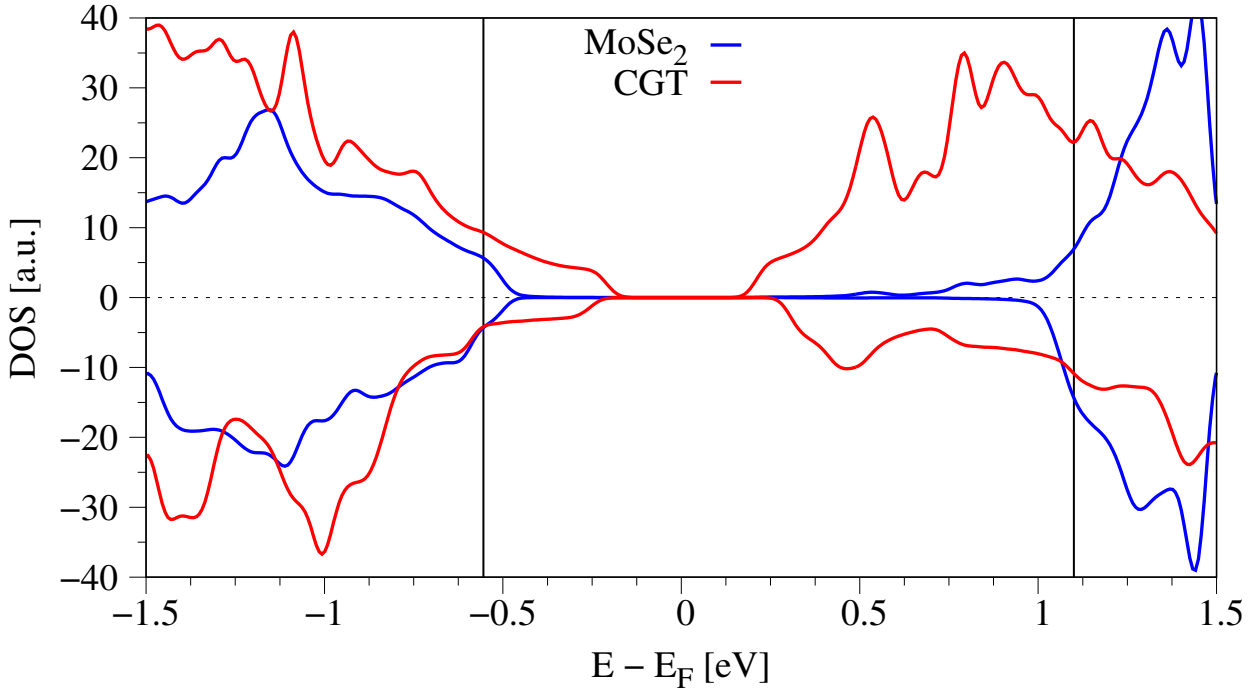

Figure S16 | The calculated layer-resolved density of states of the $MoSe_2$/bilayer-$Cr_2Ge_2Te_6$ heterostructure. Positive (negative) DOS is for spin up (down). Black vertical lines indicate the $MoSe_2$ band edges at K/K'.

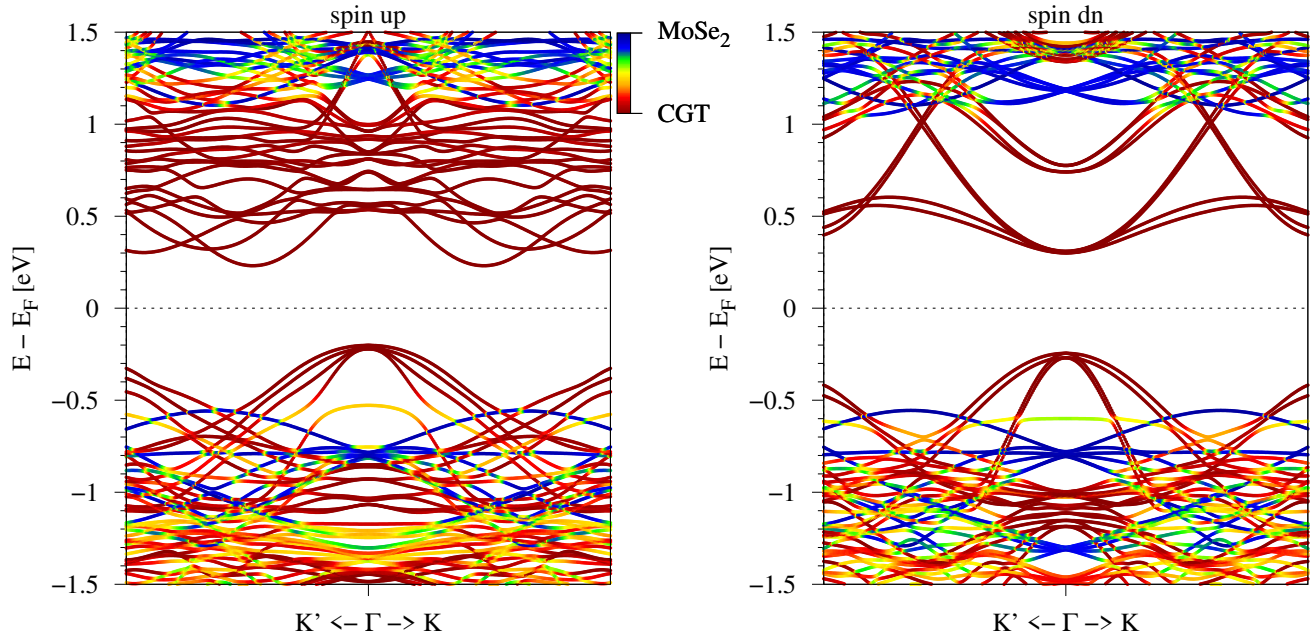

Figure S17 | The layer-projected band structure for spin up (left) and spin down (right) channels. The color code indicates the projection onto the monolayers.

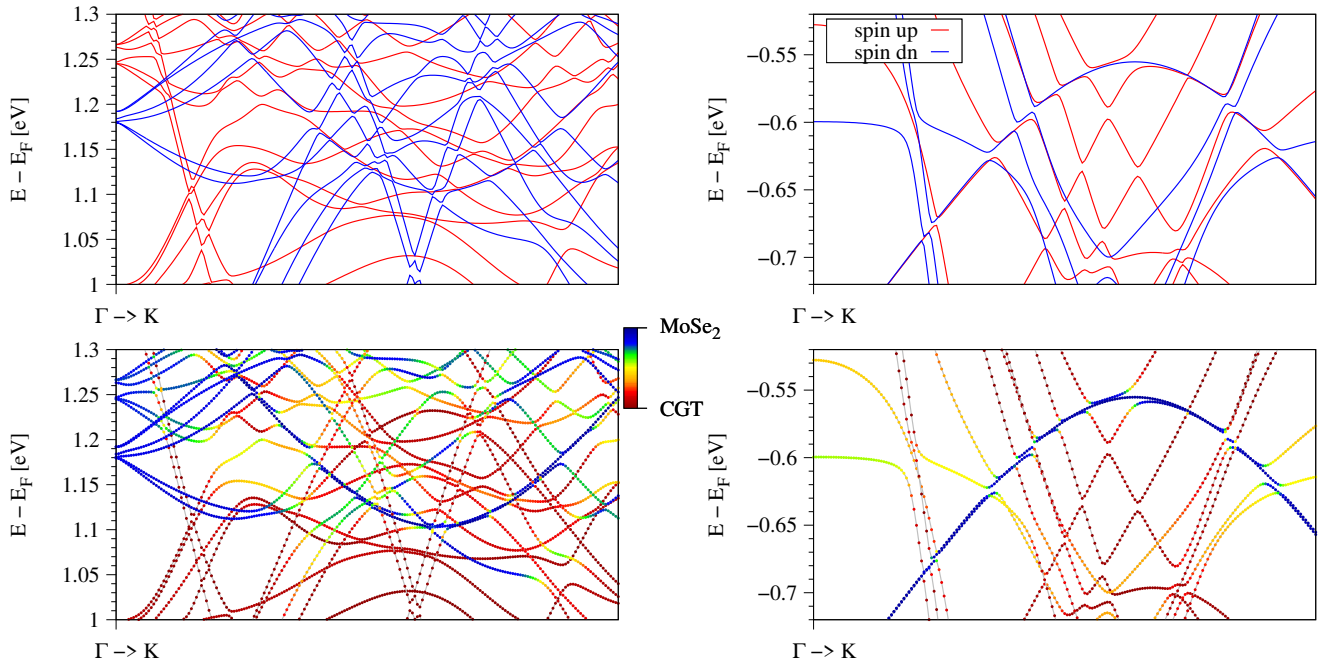

Figure S18 | Zoom to the band edges near the K-valley of $MoSe_2$.

[1] C. Gong, L. Li, Z. Li, H. Ji, A. Stern, Y. Xia, T. Cao, W. Bao, C. Wang, Y. Wang, Z. Q. Qiu, R. J. Cava, S. G. Louie, J. Xia, and X. Zhang, Discovery of intrinsic ferromagnetism in two-dimensional van der waals crystals, Nature **546**, 265 (2017).

[2] S. R. Bahn and K. W. Jacobsen, An object-oriented scripting interface to a legacy electronic structure code, Comput. Sci. Eng. **4**, 56 (2002).

[3] P. Lazic, Cellmatch: Combining two unit cells into a common supercell with minimal strain, Computer Physics Communications **197**, 324 (2015).

[4] D. S. Koda, F. Bechstedt, M. Marques, and L. K. Teles, Coincidence lattices of 2d crystals: heterostructure predictions and applications, The Journal of Physical Chemistry C **120**, 10895 (2016).

[5] S. Carr, S. Fang, and E. Kaxiras, Electronic-structure methods for twisted moiré layers, Nature Reviews Materials **5**, 748 (2020).

[6] V. Carteaux, D. Brunet, G. Ouvrard, and G. Andre, Crystallographic, magnetic and electronic structures of a new layered ferromagnetic compound $Cr_2Ge_2Te_6$, J. Phys.: Condens. Mat. **7**, 69 (1995).

[7] W. J. Schutte, J. L. De Boer, and F. Jellinek, Crystal structures of tungsten disulfide and diselenide, Journal of Solid State Chemistry **70**, 207 (1987).

[8] P. Hohenberg and W. Kohn, Inhomogeneous electron gas, Phys. Rev. **136**, B864 (1964).

[9] P. Giannozzi and et al., Quantum espresso: a modular and open-source software project for quantum simulations of materials, J. Phys.: Cond. Mat. **21**, 395502 (2009).

[10] G. Kresse and D. Joubert, From ultrasoft pseudopotentials to the projector augmented-wave method, Phys. Rev. B **59**, 1758 (1999).

[11] J. P. Perdew, K. Burke, and M. Ernzerhof, Generalized gradient approximation made simple, Phys. Rev. Lett. **77**, 3865 (1996).

[12] S. Grimme, Semiempirical gga-type density functional constructed with a long-range dispersion correction, J. Comput. Chem. **27**, 1787 (2006).

[13] S. Grimme, J. Antony, S. Ehrlich, and H. Krieg, A consistent and accurate ab initio parametrization of density functional dispersion correction (DFT-D) for the 94 elements H-Pu, J. Chem. Phys. **132**, 154104 (2010).

[14] V. Barone, M. Casarin, D. Forrer, M. Pavone, M. Sambi, and A. Vittadini, Role and effective treatment of dispersive forces in materials: Polyethylene and graphite crystals as test cases, J. Comput. Chem. **30**, 934 (2009).

[15] K. Zollner, P. E. Faria Junior, and J. Fabian, Proximity exchange effects in $mose_2$ and wse_2 heterostructures with cri_3: Twist angle, layer, and gate dependence, Phys. Rev. B **100**, 085128 (2019).